PAPER • **OPEN ACCESS**

Chemical and surface modification in graphene oxide for optimum CO_2 gas sensing performance

To cite this article: Pradeep Kumar *et al* 2025 *Nano Ex.* **6** 025004

NANO EXPRESS

PAPER

Chemical and surface modification in graphene oxide for optimum CO_2 gas sensing performance

Pradeep Kumar[1,2,7,*], **Monika Gupta**[1,2,3,7,*], **Huzein Fahmi Hawari**[1,2,4], **Vipin Kumar**[5] and **Yogendra Kumar Mishra**[6]

[1] Department of Electrical and Electronic Engineering, Universiti Teknologi PETRONAS, Seri Iskandar, 32610, Perak, Malaysia
[2] Centre of Nanostructures and Nanodevices (COINN), Division of Research, Innovation, and Commercialization, Universiti Teknologi PETRONAS, Seri Iskandar, 32610, Perak, Malaysia
[3] Naturality Research & Development SL, Terrassa, Barcelona, Spain
[4] Faculty of Electrical Engineering and Technology, Universiti Malaysia Perlis, Pauh Putra Campus, 02600 Arau, Perlis, Malaysia
[5] Department of Physics, KIET Group of Institutions, Delhi NCR, Ghaziabad, 201206, India
[6] NanoSYD, Mads Clausen Institute, University of South Denmark, Sønderborg, Denmark
[7] Authors contributed equally
[*] Author to whom any correspondence should be addressed.

E-mail: pradeepkumaruns@gmail.com

Keywords: CO_2 sensors, graphene, oxygen functional group, reduced graphene oxide, reducing agent, gas sensing, room temperature

Supplementary material for this article is available online

OPEN ACCESS

RECEIVED
19 January 2025

REVISED
18 March 2025

ACCEPTED FOR PUBLICATION
31 March 2025

PUBLISHED
14 April 2025

Abstract

The level of CO_2 gas sensing is very crucial for applications such as medical and air quality monitoring. The conventional metal oxide-based CO_2 sensors are sensitive but they need additional excitation like high temperature to be operated at room temperature. In this study, the effect of reduction time on the surface functional groups of the graphene-based sensing layer is investigated to achieve high performance of CO_2 gas sensors to be operated at room temperature. Five reduction times (20, 30, 40, 50, 60 min) are examined to synthesize reduced graphene oxide (rGO) from GO precursor material using green reducing agent ascorbic acid. The structural and morphological properties of rGO-based ArGO samples are investigated using FTIR, Raman, and SEM characterization techniques exhibiting the layered, wrinkled structure with apparent folds on the ArGO thin film surface. The highest and the lowest number of oxygen functional groups are shown by the ArGO20 and ArGO60 thin films, respectively. The electrical characterization presents the highest sheet resistance of 786 KΩ sq^{-1} and the lowest sheet resistance of 103 KΩ sq^{-1} for ArGO20 and ArGO60 thin films, respectively. Five sensors are fabricated following the reduction time to detect the CO_2 gas at room temperature. Among them, the ArGO40 sensor demonstrated optimum sensing response towards CO_2 gas with high sensitivity, repeatability, selectivity, and long-term stability, revealing that the reduction time of 40 min is optimum to synthesize functionalized graphene sensing material for CO_2 detection.

1. Introduction

The growing environmental pollution has adverse effects on human health and planet ecosystems. Continuous emission of greenhouse gases is the foremost cause of climate change, primarily driven by industrial and human activities [1, 2]. This makes monitoring air quality and implementing effective countermeasures critical for improving life on the earth. Over the past decade, greenhouse gases like carbon dioxide (CO_2) have been closely explored by researchers for their substantial impact on global warming [3–5]. Elevated CO_2 levels not only degrade environmental quality but also cause serious respiratory and cardiovascular diseases [6]. Long-term exposure to high-level CO_2 is associated with an increased risk of lung cancer which can be life-threatening, highlighting the urgent need for effective and efficient CO_2 sensing [6].

Quartz crystal microbalance (QCM) based sensors are highly sensitive and can detect a change in mass in the nanogram range. QCM oscillates at a fundamental (resonance) frequency dependent on the mass on the QCM

electrode [7]. The change in resonance frequency of the QCM sensor can be observed with the adsorption of analyte gas molecules on the sensing material coated at the QCM electrode [8]. Along with mass, other factors such as viscosity, gas pressure, elastic property of crystal, and operating temperature also impact the QCM sensor response [9]. According to the Sauerbrey equation, the frequency shift depends on the mass change when the sensing material is coated uniformly. M. Berouaken *et al* [10] reported the vanadium oxide-coated QCM sensor for CO_2 gas detection at room temperature. The thin film of vanadium oxide was deposited onto the QCM using a vacuum thermal evaporation technique followed by heating at 200 °C. They reported a frequency shift of ~17 Hz under a CO_2 gas pressure of 40mbar. Similarly, Mardiana *et al* [11] reported the titanium dioxide nanoparticle (TiO_2 NP) coated QCM sensor for CO_2 gas. They investigated the frequency shift of different concentrations of TiO_2 nanoparticles coated on the 5 MHz QCM sensor and found that the highest concentration of TiO_2 NP showed the highest frequency shift. In another work, Malhotra *et al* [12] demonstrated a novel approach to gas leak detection by incorporating a metal–organic framework (MOF) with a QCM sensor. The MOF functionalized QCM sensor was found to be selective towards CH_4 and CO_2, exhibiting distinct frequency shift for each gas without using complex calibration process. These studies show that the sensing material play a crucial role in detecting the CO_2 gas.

Various nanomaterials for CO_2 sensing have been utilized as gas sensing material [13–15]. Carbon-based materials such as graphene and its hybrids or nanocomposites have been widely explored due to their outstanding chemical and structural properties [16–19]. Pristine graphene does not have a bandgap, restricting the graphene-based gas sensor due to sp^2 hybridized carbon atoms which makes it chemically inert. Moreover, pristine graphene does not have active sites [20, 21]. As a result, the molecules of the analyte gas do not easily adsorb onto the pristine graphene surface, resulting in a low response to analyte gas [22, 23]. Alternatively, the derivatives of graphene have also been explored for CO_2 sensing.

Graphene derivative namely graphene oxide (GO) is produced by the oxidation of graphite using strong oxidizing agents like $KMnO_4$, H_2SO_4, and H_2O_2 (Hummers' method). Due to oxidation, the OFGs (such as epoxy groups, hydroxy groups, and carbonyls,) are introduced. These OFGs are covalently or non-covalently bonded with the edge and basal plane of GO sheets, making the GO hydrophilic and less agglomerated. Shaban *et al* [24] studied a GO-based gas sensor wherein, the GO-based sensing film was prepared using a modified Hummers' method. In their study, they utilized the spray pyrolysis method to prepare nanoporous graphene oxide (NGO) film sensors and showed the response of gas sensors depends on OFGs on the surface of GO-based sensing film. However, the excessive presence of OFGs at the GO surface makes it an insulating material. Thus, GO cannot be a suitable material for gas sensors. Another graphene derivative namely reduced graphene oxide (rGO) has also been explored. The rGO is produced by further reduction of GO by chemical/thermal synthesis method [25, 26] wherein, some of the OFGs are reduced after the reduction of GO. OFGs remained at the edge and basal planes; the defects formation after OFGs reduction, and the type of OFGs left after the reduction process decide the performance of a gas sensor. Hydroxyl OFGs are mainly attached to the basal plane whereas the carbonyl and carboxyl groups are attached to the edge plane [27]. Although both edge and basal plane OFGs play crucial roles in gas adsorption, the basal plane OFGs work as the trap sites, resulting in the baseline drift of the gas sensor [17].

The amount of OFGs at the rGO surface depends on the reduction process. The reduction of OFGs present at the GO surface leads to some residual oxygen which tends to trap electrons, thereby holes generated in the rGO lattice [28]. The dominancy of hole charge carriers on the rGO surface makes it, a p-type semiconductor [29–31]. The surface properties of GO can be easily modified by changing chemical reduction parameters such as the type of reducing agent [27, 32, 33], and the reduction temperature [34]. Different reducing agents have been explored to modify the surface property by varying the functional groups [35]. For example, Lesiak *et al* [36] reported distinct modifications in the chemical and structural properties of rGO using reducing agents such as sodium borohydride ($NaBH_4$), hydrazine (N_2H_4), sodium hydroxide (NaOH), formaldehyde (CH_2O) and L-ascorbic acid ($C_6H_8O_6$). In another report, Chen *et al* [32] utilized reducing agents such as hydrazine monohydrate, and ascorbic acid to functionalize the GO and found that AA removes OFGs such as epoxide and hydroxyls and increases the presence of carbonyl and carboxyl FGs. The AA reduced GO showed the formation of new graphitic domains with small spatial dimensions. The aforementioned reducing agents except ascorbic acid are very toxic and hazardous whereas ascorbic acid is a green reducing agent [27].

The duration of the chemical reduction process also plays a key role in modifying the surface properties of GO [37]. However, it is found that no previous studies have been conducted to observe the effect of the reduction time of GO using ascorbic acid on the performance of CO_2 gas sensors. In this study, a high-quality functionalized graphene with desired surface properties is produced by tuning the OFGs by carefully optimizing the reduction time. Ascorbic acid is used to reduce the GO for a small duration range (20 min, 30 min, 40 min, 50 min, and 60 min) of synthesis to achieve optimum OFGs on its surface with good electrical conductivity in order to realize highly sensitive CO_2 sensor showing fast response at room temperature.

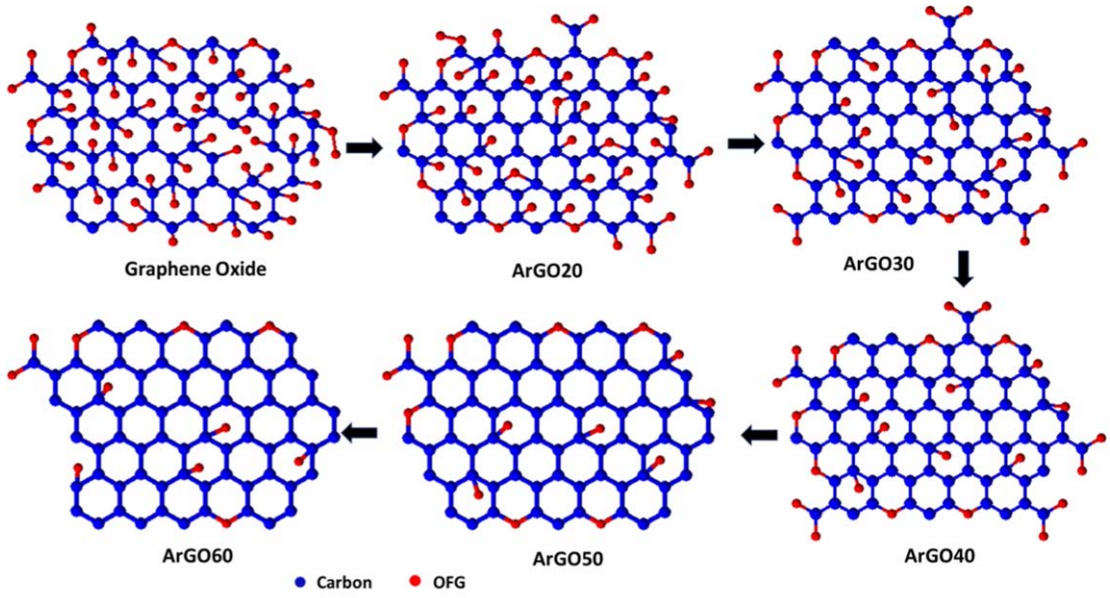

Figure 1. Schematic illustration of GO, ArGO20, ArGO30, ArGO40, ArGO50, and ArGO60, representing structures of rGO after synthesis duration of 20, 30, 40, 50, and 60 min, respectively, using ascorbic acid reducing agent.

2. Materials and methods

2.1. Materials and reagents

Graphene oxide (GO) paste (95%) was purchased from Graphenea (San Sebastian, Spain). The CO_2 gas cylinder (500 ppm concentration) was purchased from Linde Malaysia Sdn. Bhd. with balancing gas of nitrogen. Ascorbic acid (AA), ethanol (95%), and acetone (95%) were purchased by Sigma Aldrich, USA. All the chemicals were of analytical grade, no further purification was required for conducting experiments. Deionized water (DI) was used in material suspension preparations.

2.2. Synthesis of reduced graphene oxide and thin-film development

To prepare the reduced-graphene oxide (rGO), an aqueous suspension of GO was initially prepared by dissolving GO paste (4 mg ml^{-1}) in DI water followed by ultrasonication for 15 min to obtain a uniform suspension. Then, 50 mg of AA concentrations were added to the GO suspension. The suspensions were prepared by slowly and carefully adding the ascorbic acid into the aqueous GO suspension. The prepared mixture was then vigorously stirred on the hot plate at 65 °C under room environment conditions. Five different rGO samples denoted as ArGO20, ArGO30, ArGO40, ArGO50, and ArGO60 were synthesized following the reduction time range of 20–60 min with intervals of 10 min. The schematic illustration of the chemical structures of ArGO samples is shown in figure 1.

The thin films of synthesized ArGO suspensions were developed by drop-casting technique. Prior to thin-film development, the target substrates such as glass and SiO_2 (300 nm)/Si were sequentially washed in acetone, isopropyl alcohol, DI water, and ethanol solvents using ultrasonication for 15 min in each solvent.

2.3. Structural, elemental, morphological, and electrical characterizations

The functional groups of the synthesized materials were investigated using attenuated total reflection Fourier Transform Infrared (ATR-FTIR) spectroscopy (Bruker Instruments, Model Aquinox 55, Stuttgart, Germany). The crystal structure of the material samples was examined using Raman spectroscopy (Horiba Jobin Yvon HR800) at ambient temperature with 514 nm laser excitation for 200–4000 cm^{-1} spectrum regions. The surface morphology of the samples was investigated using scanning electron microscopy (*SEM*, Leo 1430vp). The sheet resistances of thin films of prepared materials were measured using a four-point probe system (Lucas Lab 302) with a Keithley 2400 source meter. The thin films of all materials were prepared onto the glass and SiO_2 substrates.

2.4. Sensor fabrication and device performance

The AT-cut 10 MHz quartz crystal microbalance (QCM, WTL International China) with silver (Ag) electrode was used as a sensing platform. QCM resonators were cleaned in acetone, isopropyl alcohol, DI water, and

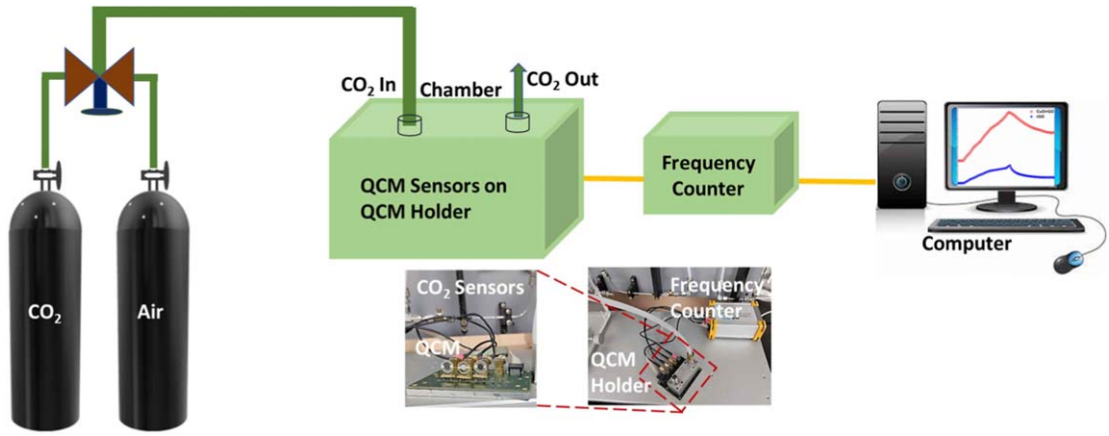

Figure 2. Schematic illustration of experimental set-up for CO_2 sensing, displaying CO_2 sensors, QCM holder, and frequency counter in the photographic view.

ethanol solvents using ultrasonication for 15 min in each solvent. A drop-casting technique was used to prepare the thin films of the sensing material on the QCM electrode. 10 μl of GO and ArGO suspensions were taken using a micropipette to drop-cast the QCM substrates on both sides under identical conditions. The material-coated QCMs were then dried at room temperature.

An uncoated QCM was tested for CO_2 gas and no response was observed for the same. The gas sensing experiments were performed by using a custom-made gas sensing setup at room temperature (figure 2). The ArGO-coated QCM resonators were placed in a QCM holder. Then, the QCM holder was connected to a frequency counter (FQ4, JLM Innovation Denmark). The output of the frequency counter was given to a compatible computer via RS–232 serial communication port to acquire the sensing performance. During testing, the air was first purged to ArGO-coated QCM for 60 s. After that, the air was turned off, and the ArGO-coated QCM surface was immediately purged of CO_2 gas (500 ppm). In the meantime, the air was purged again in order to desorb (remove) the CO_2 gas molecules. The adsorption and desorption of CO_2 molecules cause a modulation in the QCM frequency. The frequency shifts quickly as the gas gets adsorbed on the ArGO-coated QCM sensor surface, and these frequency shifts were recorded using a frequency counter. The timeframes required for the sensor to reach 10% and 90% of the maximum shifts during the sensing and purging procedures, respectively, were used to calculate the response and recovery times.

3. Result and discussion

3.1. Functional group analysis

The structural properties of GO and ArGO samples were studied using FTIR spectroscopy. The ATR-FTIR analysis was conducted using powdered GO and rGO samples. The powders were directly placed on the ATR crystal and gently pressed using the built-in pressure clamp of the instrument to ensure optimal contact with the crystal. This approach minimizes sample preparation complexity and avoids additional effects from substrates or matrix materials. The FTIR spectra of ArGO samples ArGO20, ArGO30, ArGO40, ArGO50, ArGO60, and GO are presented in figure 3. The GO spectrum showed a broad absorption band centered at 3182 cm^{-1} (E) attributed to the −OH stretching vibration and indicating the presence of -OH and -COOH- functional groups within the structure. The peaks at 1724, and 1620 (D) cm^{-1} were detected suggesting the vibrations of C=O stretching, and C=C alkene group stretching. Some other peaks at 1225 and 1044 cm^{-1} (A) were observed indicating the C–O stretching of epoxy groups and the C–O stretching vibration of an alkoxy group, respectively. In the ArGO spectra, it was noticed that the peak intensity of most of the oxygen functional group (OFGs) was found to be decreased which indicates the successful reduction of graphene oxide by AA reducing agent. It was also observed that the peaks due to the hydroxyl group were absent at ~3182 cm^{-1} in all the ArGO samples. After 30 min of reduction (ArGO30), the absorption peak at ~1580 cm^{-1} emerged which indicates the successful deoxygenation of the ArGOs by AA. However, the absence of any peak at ~1580 cm^{-1} in the ArGO20 sample, is attributed to the partial reduction of GO and almost negligible restoration of the C=C bonds. Meanwhile, the intensity of ~1580 cm^{-1} peak decreased further from ArGO40 to ArGO60.

The peak at ~1228 cm^{-1} (B), and ~1720 cm^{-1} corresponded to stretching vibrations from epoxy C–O, and carbonyl C=O. These peaks were absent in the ArGO20 sample indicating the negligible sp^2 hybridization of the C–O bond in the basal plane. However, these peaks existed in the samples ArGO30 to ArGO60 with their highest

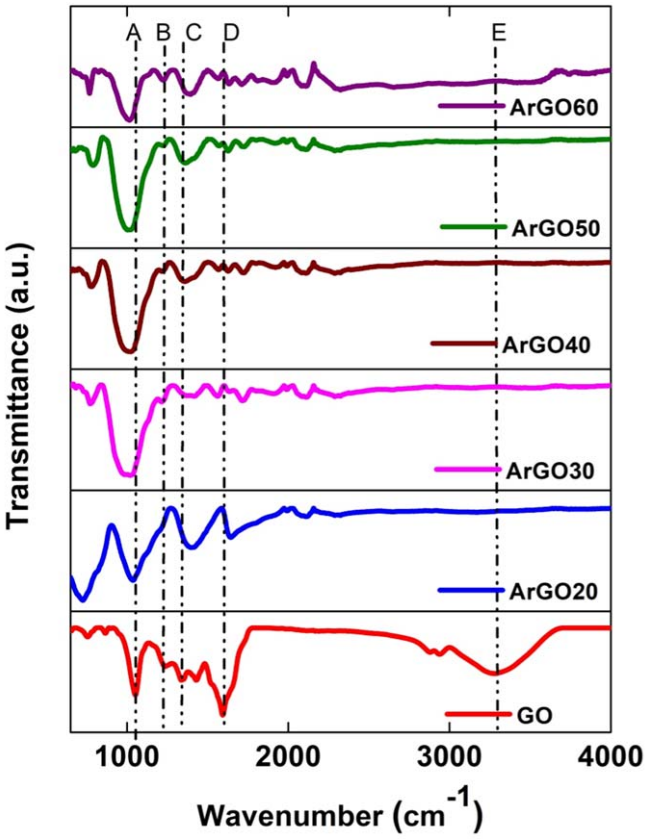

Figure 3. FTIR spectra of GO, ArGO20, ArGO30, ArGO40, ArGO50, and ArGO60, indicating a continuous decrease in the intensities of the peaks with increasing reduction time from 20 min to 60 min with intervals of 10 min. Functional groups C–O–C, C–O, C=O, C=C, –OH represented by A, B, C, D, and E.

intensity in the ArGO60 sample. The peak at ~1380 cm^{-1} (C) corresponds to carboxyl C=O symmetric stretching vibrations, the highest intensity was observed in the ArGO20 sample, and the lowest intensity was observed in ArGO30.

During the reduction process of GO to rGO, a decrease in peak intensities of FTIR bands represented the presence of OFGs in all samples. To monitor the reduction degree and to investigate the change in the bond nature of carbon and oxygen, the area under the peaks for the wavenumbers from 1044 cm^{-1} to 1438 cm^{-1} was estimated (figure S2). The wavenumber band 1044–1438 cm^{-1} exhibits most of the edge plane OFG peaks. A deconvoluted FTIR spectrum for this band was used to analyze the percentage reduction (figure S1) where one broad peak and three small peaks were obtained. The wider peak at ~1044 cm^{-1} is attributed to epoxide C-O stretching vibration as a result of hydroxyl transfer to the epoxide during the reduction process. Thus, epoxide OFGs have been selected to investigate the reduction degree in this study. Moreover, the reduction efficiency is calculated by utilizing the area under the band 1044–1438 cm^{-1} (equation (1)) [38].

$$Reduction\ Efficiency = \frac{A_{GO}}{A_{rGO}} \times 100 \quad (1)$$

Where A_{GO} and Ar_{GO} are the areas under the wavenumber band for GO and rGO respectively. An increase in reduction efficiency was observed upon increasing the duration of the reduction process. After reduction, the area under these peaks reduced significantly which implies a reduction of the OFGs. The reduction efficiency of all samples was in the order of ArGO20 (~89%) < ArGO30 (96%) < ArGO40 (~97.1%) < ArGO50 (~97.6%) < ArGO60 (~98.1%). The comparison shows that the reduction of OFGs occurs majorly in the early 30 min.

3.2. Structural analysis

The structure configuration of rGO samples was investigated by Raman spectroscopy, as shown in figure 4, showing significant two bands ~1350 cm^{-1} and ~1600 cm^{-1} termed as D band and G band, respectively. The D band is assigned to the structural imperfections or defects that occur due to hydroxyl and epoxide functional groups on the basal plane [39]. The G band is attributed to the first-order scattering of the E_2g phonon vibration from sp^2 carbon and can be observed for all carbon materials containing sp^2 carbon structure [40]. Both bands

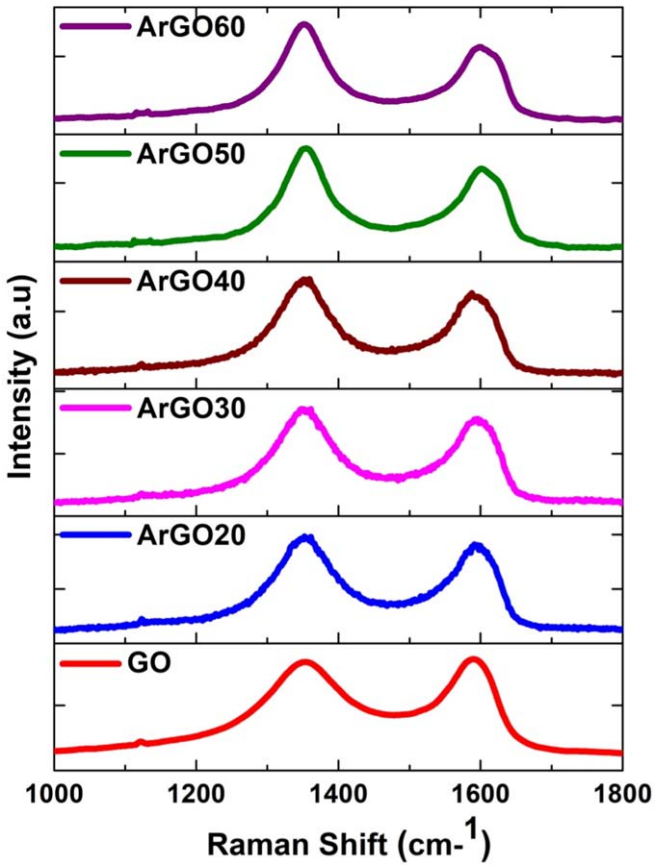

Figure 4. Raman Spectra (D, G peaks) of GO, ArGO20, ArGO30, ArGO40, ArGO50, ArGO60, indicating a red shift in D-peaks and a blue shift in G-peaks of ArGO samples with increasing duration of reduction process.

were found to be broad, suggesting the presence of imperfections and OFGs in all samples. The intensity and FWHM of the D band depend on defects, disorders, and type of edges. The existence of a higher intensity of the D band indicates armchair defects rather than zigzag defects or edges [38]. The intensity ratio of D to G peak (ID/IG) was found in the order GO (0.97) < ArGO20 (1.071) < ArGO30 (1.12) < ArGO40 (1.18) < ArGO50 (1.259) < ArGO60 (1.29). This order suggests that the armchair edge defects increase with increasing reduction duration. For Raman analysis, three points were chosen in each sample for testing. The variation in I_D/I_G ratio is shown in figure S3.

The I_D/I_G ratio increased significantly as reduction time increased, showing an improved degree of reduction with time. Also, the increased I_D/I_G ratio was attributed to a decrease in the average size of the sp^2 graphitic domain and defect density, suggesting, that the smaller size new graphitic domains were generated as compared to GO [41, 42]. The increase in defectiveness enhances the surface reactivity and provides additional adsorption sites for gas absorption. Thus, more gas molecules will interact with the rGO surface to provide higher sensing performance. As the reduction duration is increased the OFGs are reduced but a higher I_D/I_G ratio is observed. This is found in agreement with the Tuinstra and Koening (TK) relationship that indicates an increased I_D/I_G ratio in highly disordered graphene [43].

Figure 5 shows the 2D and D+G peaks of samples GO, ArGO20, ArGO30, ArGO40, ArGO50, and ArGO60 found at Raman shift ~2700 cm^{-1} and ~2900 cm^{-1}, respectively. The 2D peak was less intense as compared to the D peak and G peak, indicating the defective nature of GO after reduction. The intense and narrow 2D peak of samples ArGO50 and ArGO60 indicates the existence of a smaller number of OFGs and the highly disordered nature of rGO as compared to other samples. The number of graphene layers was determined by the shape, size, and position of the 2D band. The intensity ratio of 2D to G peak (I_{2D}/I_G) was in the order of 0.282 (ArGO20), 0.288 (ArGO30), 0.175 (ArGO40), 0.216 (ArGO50), and 0.197 (ArGO60). The Raman spectra of ArGO20 and ArGO30 samples have few-layer graphene and ArGO40, ArGO50, and ArGO60 samples have a 2D shape characteristic of multilayer graphene. The I_{2D}/I_G ratio determines the number of layers in the graphene sheet [44]. The narrow and sharp 2D peak has a smaller number of layers. It has been observed when the G band increases, the 2D band decreases. Thus, the number of layers in graphene is assumed to be decreased. As the number of layers decreases, the 2D peak becomes sharp, symmetric, and increases in intensity which confirms

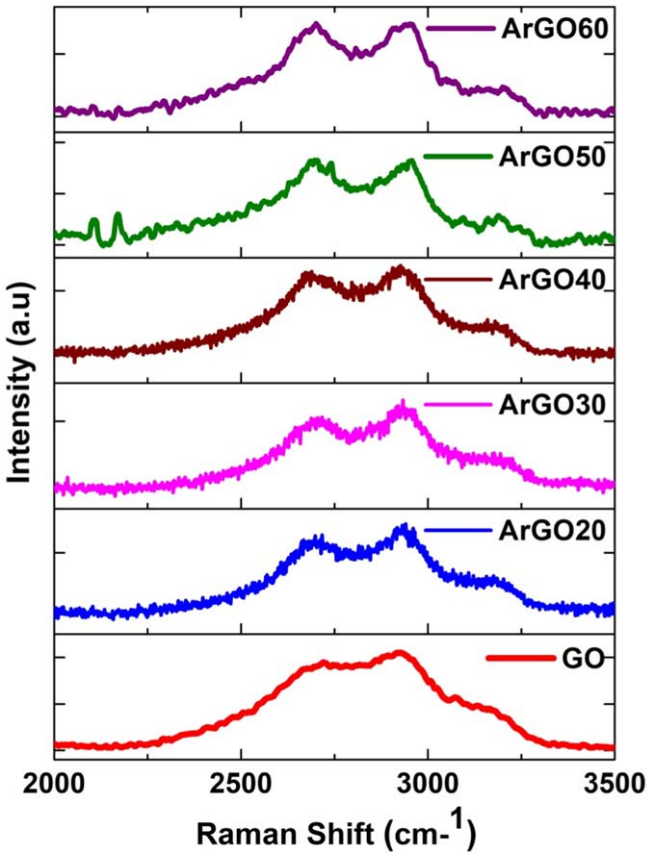

Figure 5. Raman spectra (2D, D+G Peak) of GO, ArGO20, ArGO30, ArGO40, ArGO50, ArGO60.

Table 1. Raman fingerprints: I_D/I_G, crystallite size L_a, average defect distance L_D, and defect density n_D for GO, ArGO20, ArGO30, ArGO40, ArGO50, and ArGO60 samples.

Sample	I_D/I_G	L_a (nm)	L_D (nm)	n_D (x 10^{11}) (cm^{-2})
GO	0.9734	1.33	13.12	3.35
ArGO20	1.071	1.39	12.5	3.68
ArGO30	1.127	1.43	12.19	3.87
ArGO40	1.18	1.46	11.91	4.05
ArGO50	1.259	1.51	11.5	4.33
ArGO60	1.298	1.53	11.36	4.46

the high electrical properties of graphene material. Raman spectra can determine the number of layers, defects, and electrical properties of graphene [45].

The D, G, and 2D peaks were also used to determine various other properties of the material such as crystallite size, defect distance, and defect density. The effective crystal size L_a (equation (2)) of the graphite plane is inversely proportional to the intensity of the D to G peak as proposed by Ferrari and Robertson [45, 46]:

$$I_D/I_G = C'(\lambda)L_a^2 \tag{2}$$

Where C' (514 nm) is ~0.55 nm^{-2}. The parameters I_D/I_G, crystallite size L_a, average defect distance L_D, and defect density n_D ($L_D \sim 1/\sqrt{n_D}$) for all the investigated samples are shown in table 1. The de-convoluted D and G peaks of the Raman spectrum for all samples are shown in figure S4. GO and all rGO samples displayed high defect density with high intensities of characteristic peaks and width of FWHM of D and G peaks but the 2D peak exhibited low intensity with I_D/I_G ratio close to unity. Moreover, the variation in position, intensity, and FWHM of D peak, G peak, and 2D peak for all rGO samples have different C_{sp3} content, crystallinity, defect distance, and graphitic size. The rGO samples were more crystalline than GO, particularly the ArGO60 sample showed the highest crystallinity.

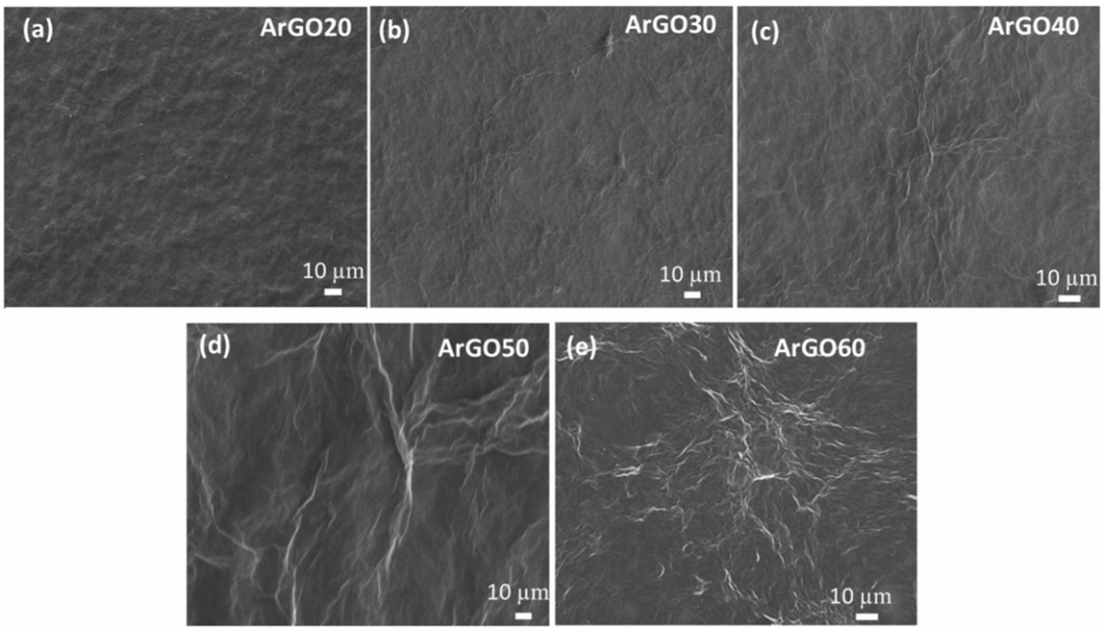

Figure 6. SEM images of (a) ArGO20, (b) ArGO30, (c) ArGO40, (d) ArGO50, and (e) ArGO60, indicate the increased wrinkles and folds with the increase in reduction duration.

L_a of all rGO samples was found to be in the nm scale further validating the presence of nanoscale domains within the rGO sheets. Moreover, L_D in the nm scale reflects a balance between defect sites and conductive domains which supports charge transport along with chemical reactivity. Thus, all the rGO samples ensure effective charge transfer upon analyte adsorption, leading to significant changes in electrical properties. The defect density (n_D) of ArGO samples was found to be relatively high, showing ample active sites such as vacancies, and edges in carbon lattice for enhanced gas adsorption.

3.3. Surface morphology

The SEM images of ArGO20, ArGO30, ArGO40, ArGO50, and ArGO60 sensing thin films are shown in figures 6(a)–(e). Some layered wrinkled structures with apparent folds were observed on the ArGO thin film surface. The wrinkled structures of the ArGO surface contribute to the high surface area which provides better reactivity for analyte gas adsorption and results in sensitive sensor material. Moreover, the interconnection between graphene layers facilitates electron transport which results in a change in electrical parameters on analyte adsorption and results in faster response time. Thin films of ArGO20 and ArGO30 were found to have less wrinkled and negligible folds (figures 6(a), (b), indicating a small surface area whereas ArGO40 was noticed to have moderate wrinkles and some folds as shown in figure 6(c). The ArGO50 and ArGO60 thin films showed comparatively more wrinkles and folds, resulting in high surface area which can facilitate analyte gas adsorption.

3.4. Surface conductivity

The sheet resistance of the ArGO thin films was measured using a four-point probe. The ArGO20 thin film showed the highest sheet resistance (786 kΩ sq^{-1}) whereas the ArGO60 thin film displayed the lowest sheet resistance (103 kΩ sq^{-1}) as shown in figure 7. The sheet resistance was found to decrease with the increase in reduction duration. This can be understood from their FTIR spectra wherein, the ArGO20 sample showed its partial reduction (partial deoxygenation) and had the highest number of OFGs at its surface, resulting in the highest sheet resistance whereas the ArGO60 sample was found to have the lowest number of OFGs at its surface, resulting in the lowest sheet resistance.

3.5. Gas sensor performance

The sensing responses of uncoated QCM and ArGO-coated QCM resonators (ArGO-based sensors) were examined by placing these resonators in a metal chamber. After that CO_2 gas was purged at room temperature in lab ambient conditions. The uncoated QCM resonator had no significant response to CO_2 gas of 500 ppm, the response of the uncoated QCM sensor is shown in figure S6. Figures 8(a)–(e) show the frequency shifts of ArGO20, ArGO30, ArGO40, ArGO50, and ArGO60 sensors, respectively. It illustrates the sensor's sensitivity and dynamic response to the CO_2 gas exposure. Each distinct frequency shift (rise and fall) likely corresponds to

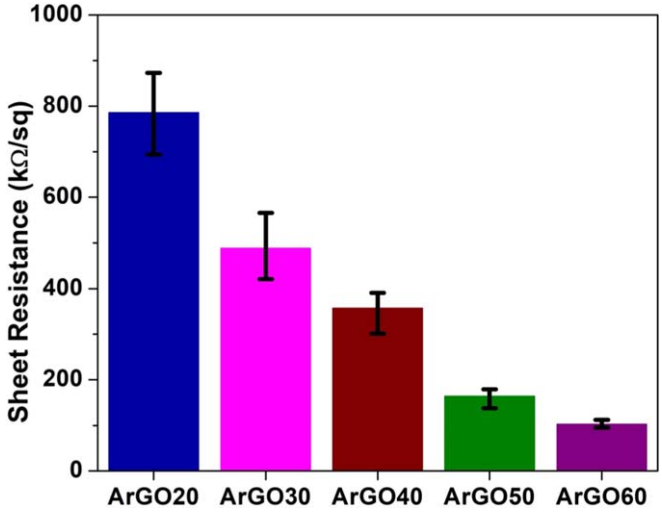

Figure 7. Sheet Resistance of ArGO20, ArGO30, ArGO40, ArGO50, and ArGO60 thin films, showing a decrease in the sheet resistance of films with the increase in the reduction duration.

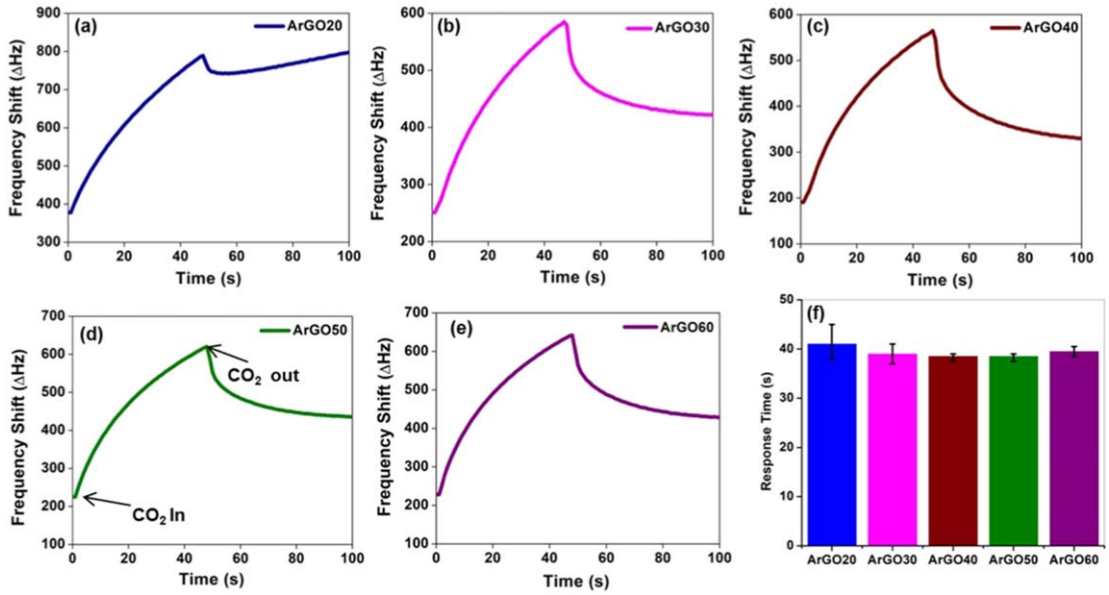

Figure 8. Response/recovery curves of (a) ArGO20, (b) ArGO30, (c) ArGO40, (d) ArGO50, (e) ArGO60 sensors for CO_2 gas (500 ppm), and (f) comparison of their response time.

a CO_2 gas exposure and removal cycle, respectively. All five sensors were sensitive to CO_2 gas (500 ppm) along with baseline drift (BLD). Moreover, all the sensors demonstrated fast response times. A comparison of their response time is shown in figure 8(f), wherein, the response time of ArGO20, ArGO30, and ArGO60 sensors were found to be 41 s, 39 s, and 39.5 s, respectively. Both ArGO40 and ArGO50 sensors showed response times of 38.5 s towards CO_2 gas at RT. The recovery time of all the sensors was also calculated and shown in figure S5. The ArGO20 sensor showed the highest recovery time of 44.5 s whereas the ArGO30 and the ArGO40 sensors displayed the low recovery time of 26 s and 28 s respectively. Figure 9 shows the repeatable response and recovery curves of ArGO-based CO_2 sensors over time for all samples. The change in frequency (response) of the sensors is depicted in figure 10 for all three repetitive cycles. This indicates the ArGO sensor's repeatable response and recovery behaviors. It was evident that the response curve of ArGO sensors has a rapid and sharp rise in frequency upon CO_2 gas exposure whereas the recovery curve has a slower and gradual decrease in frequency towards baseline with each cycle upon CO_2 removal.

The sensor ArGO20 demonstrated a frequency shift of 411 Hz which was very close to the obtained frequency shifts of ArGO50 and ArGO60 sensors. Moreover, the ArGO20 sensor also showed the highest BLD. The high response of the ArGO20 sensor is possibly due to the highest number of OFGs (basal plane and edge

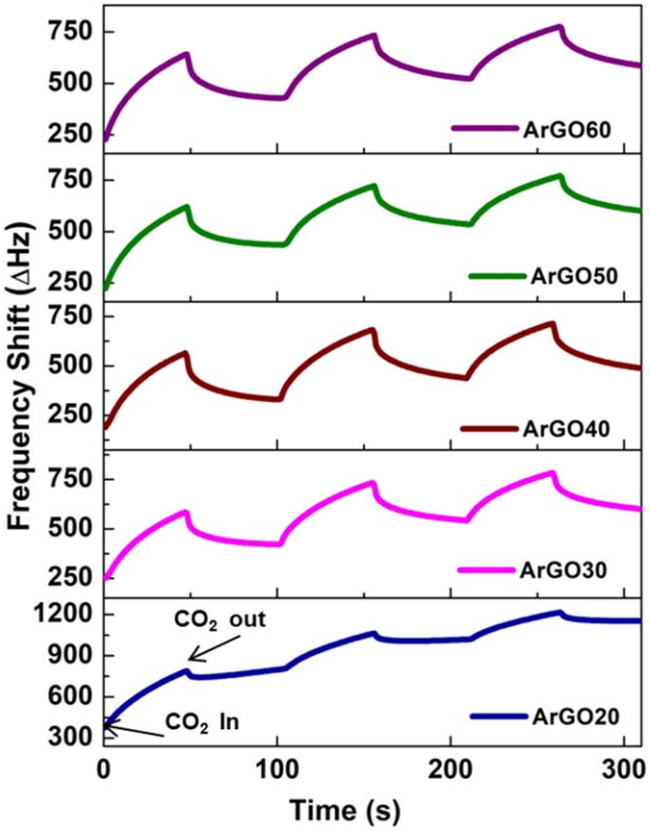

Figure 9. Repeatability curve of ArGO20, ArGO30, ArGO40, ArGO50, and ArGO60 sensors for 500 ppm CO_2.

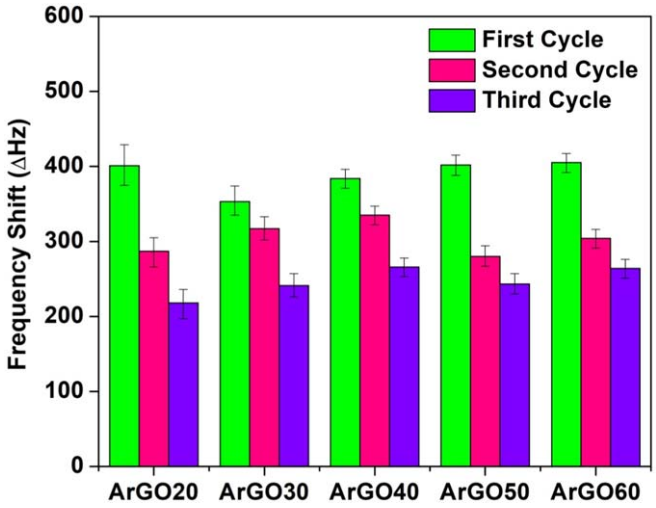

Figure 10. Response of all the three repeated cycles for ArGO20, ArGO30, ArGO40, ArGO50, and ArGO60 sensors.

plane) present at the ArGO20 surface but the highest BLD is due to basal plane trap charge OFGs. The response of ArGO20 was further reduced in repeated pulses due to the memory effect (BLD). The response of ArGO40 was found to be the highest and decreased slightly (5%) in the second cycle. The response of ArGO30 was found to be the smallest for the first cycle but for the second repeated cycle only a 7% decrease was observed, whereas the ArGO60 sensor shows a ~25% decrease and the ArGO50 sensor shows a ~27% decrease in response at the second repeated cycle as shown in figures 10(a)–(c).

Figure 11 depicts the baseline drift (BLD) of all the prepared sensors. The BLD over each cycle suggests a swelling and persistent effect on the ArGO sensor response. This may be due to the active sites (OFGs) present at the basal plane of the graphene surface because OFGs present at the basal plane work as trap sites for the charge

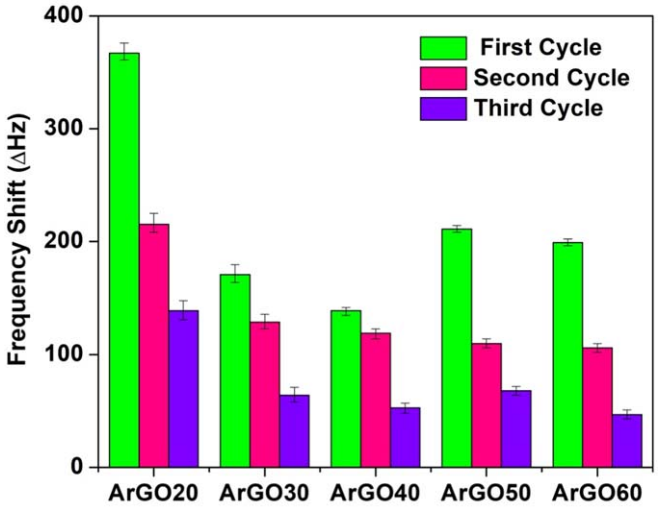

Figure 11. Baseline drift of all the three repeated cycles ArGO20, ArGO30, ArGO40, ArGO50, and ArGO60, sensors.

carriers. These trap sites are constantly increasing with each adsorption/desorption cycle because of incomplete desorption of CO_2 molecules after each cycle which in turn increases the hole concentration. The CO_2 molecule is a strong acceptor, and it leaves a hole at the sensor surface upon desorption. Therefore, the hole carrier concentration is increased at the surface and this excessive hole carrier concentration reduces gradually the CO_2 gas reactivity with the surface which results in an upward shift in the ArGO sensor baseline, which is visible in the response of ArGO20, ArGO30 sensors (figures 8(a) and (b)).

The BLD has a direct impact on sensor performance by altering sensor performance metrics such as accuracy, stability, and repeatability. BLD is an indicative measure to understand the stability of a sensor. It was evident that ArGO20 was highly unstable while ArGO40 had good stability because of the smallest BLD. The ArGO20 sensor showed the highest BLD after each cycle, particularly 367 Hz after the first cycle, 215 Hz after the second cycle, and 139 Hz after the third cycle. The repeatability and reproducibility of the ArGO20 sensor were difficult to realize after multiple measurements, due to its high BLD. On the contrary, the ArGO40 sensor realized the smallest BLD due to the availability of active sites such as vacancies and functional groups at the edge plane. The responses of the ArGO30, ArGO50, and ArGO60 sensors were comparable to the ArGO40 sensor but BLD was found to be higher in the ArGO30 sensor compared to ArGO40. The sensors having high BLD show inconsistent sensor performance under the same environmental conditions which makes these sensors unreliable in applications where precise measurement is crucial for example, medical diagnostics. Therefore, ArGO50 and ArGO60 can be the best choice for medical applications. Moreover, significant BLD results in slower response and recovery time of the sensor due to persistent memory effect that prevents the ArGO sensor from fully returning to its baseline thereby restricting the long-term stability of the sensor. From figures 10 and 11, it can be evident that ArGO40 has the highest response and the lowest BLD which confirms that ArGO40 was the best sensor with good sensitivity, stability, repeatability, reproducibility, and long-term stability.

The selectivity test of the ArGO40 sample was also investigated to discriminate between analyte and interfering gases. Figure 12 shows the sensor's response to acetone, ethanol, toluene, and CO_2 at concentrations of 500 ppm. The selectivity indicates the ability to distinguish target gas from interfering gas which can be quantitatively expressed by the ratio of the sensor response towards the specific gas (CO_2) to that of interfering gases (acetone, ethanol, toluene,). This ratio is also termed as selectivity coefficient or selectivity index [47]. The selectivity coefficient of the ArGO40 sample was found to be 7.5 for acetone, 3.67 for toluene, and 4.69 for ethanol which shows the lowest change in frequency for acetone.

It was found that the ArGO40 sample shows the highest shift in frequency for CO_2 gas. Moreover, the baseline drift of ArGO40 was found to be lowest for CO_2 gas as compared to acetone, ethanol, and toluene as shown in figure 12(b). CO_2 gas has a strong affinity for OFGs such as –OH, -C=O, and –C-O-C due to dipole interactions and form Lewis acid–base interactions. The CO_2 molecules have a small structure as compared to polar organic molecules; small molecules can penetrate the rGO surface effectively and get adsorbed in larger quantities, leading to significant frequency shifts. However, polar organic molecules such as acetone, ethanol, and toluene primarily interact via weak van der Waals forces or hydrogen bonds and this adsorption/desorption is not as strong/quick as rGO has with OFGs, contributing small change in frequency.

The long-term stability of the ArGO40 sample is shown in figure 12(c). The same ArGO40 sample was tested for 60 days maintaining the same lab conditions (RT = 25 °C and 58% RH). It can be observed that after day 5

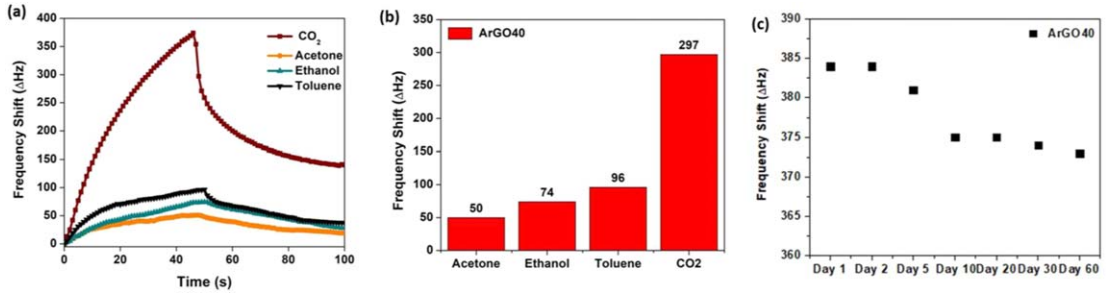

Figure 12. Selectivity test - (a) gas response and (b) frequency shift of ArGO40 sensor for acetone, ethanol, toluene, and CO_2 gas, exhibiting the highly selective ArGO40 sensor sample towards CO_2 gas at RT, and (c) stability of ArGO40 sensor for 60 days. The same sensor is tested towards 500 ppm CO_2 gas under the same laboratory conditions at room temperature.

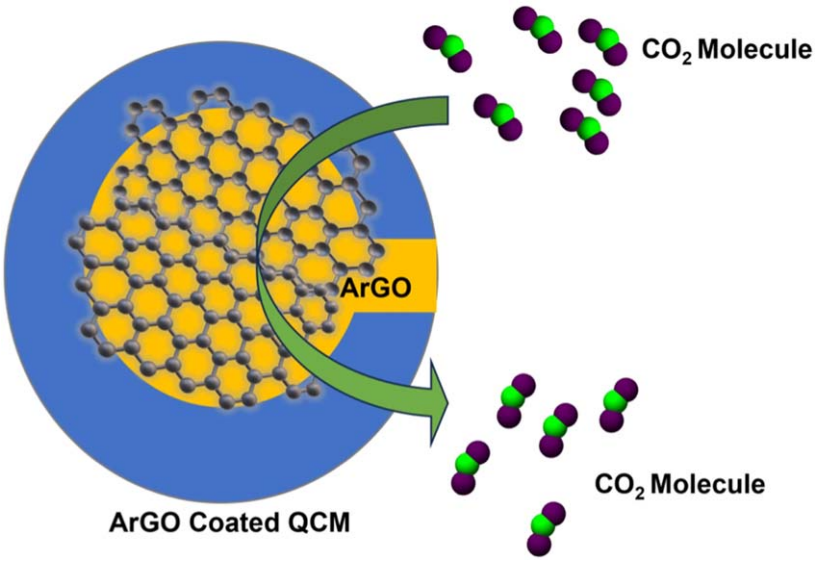

Figure 13. Schematic illustration of CO_2 gas molecule adsorption on the surface of ArGO surface.

there is a slight decrease in sensor response and becomes almost constant till day 60. Thus, the ArGO sensor shows good long-term stability. The effect of humidity on the ArGO40 sensor was also investigated and shown in figure S7. The response of CO_2 is enhanced under humid conditions similar effects were observed with the ArGO40 sensor.

Figure 13 shows the possible CO_2 gas-sensing mechanism of the ArGO sensor. When the synthetic air is purged on the ArGO sensor, the oxygen molecules get adsorbed on the ArGO surface by the physisorption process due to van der Waal and dipole interactions at room temperature [48]. By trapping a free electron from the ArGO surface, the adsorbed oxygen molecule is subsequently ionized to oxygen ions O_2^- [49]. These oxygen ions form a layer at the ArGO surface interact with CO_2 molecules upon exposure to CO_2 gas and form the carbonate ions [10, 50]. The reaction process is given below,

$$O_2 + e^- \leftrightarrow O_2^-(ads) \tag{3}$$

$$O_2(ads) + e^- \leftrightarrow O_2^-(ads) \tag{4}$$

$$CO_2(gas) \leftrightarrow CO_2(ads) \tag{5}$$

$$2CO_2(gas) + O_2^- + e^- \leftrightarrow 2CO_3^-(ads) \tag{6}$$

4. Conclusion

In this work, we optimized the reduction time of precursor GO using green reducing agent ascorbic acid by following the chemical solution-processed method for rGO synthesis. The effect of the reduction time of GO on the structural and surface properties (OFGs, sheet resistance) as well as related CO_2 sensing performance was

investigated in detail. Five reduction times 20 min, 30 min, 40 min, 50 min, and 60 min were used to modify the OFGs in order to maintain the edge plane active sites. FTIR analysis of all ArGO samples revealed that the numbers of OFGs decreased with the reduction time. An increase in reduction efficiency (89% to 98%) was observed upon increasing the reduction time from 20 min to 60 min. The Raman analysis ensured the chemical reactivity of ArGO surfaces. It was discovered that the increase in the I_D/I_G intensity ratio and defect density with an increase in the reduction time. SEM microscopy exhibited an increase in the layered, wrinkled structures and apparent folds in the ArGO thin film surface with an increase in the reduction time. The structural and morphological properties of ArGO samples using FTIR, Raman, and SEM characterization techniques showed that the ArGO20 thin film has the highest number of OFGs whereas the ArGO60 thin film has the lowest number of OFGs. From electrical characterization, the highest and lowest sheet resistance of ~786 KΩ sq^{-1} and ~103 KΩ sq^{-1} were measured for ArGO20 and ArGO60 thin films, respectively. The sensing results revealed that all ArGO sensors were found to be sensitive towards CO_2 gas. The ArGO40 sensor revealed a high response for all repeatable pulses with the lowest baseline drift. The BLDs of ArGO60 and ArGO50 were comparable to the ArGO40 sensor but the responses of ArGO60 and ArGO50 were found to decrease by 25% and 27%, respectively for the second pulse. The ArGO20 and ArGO30 sensors showed comparatively higher baseline drifts. This study suggested that the optimum reduction time was 40 min to achieve optimum sensing response towards CO_2 gas with good sensitivity and repeatability. ArGO40 sensor was found to be selective towards CO_2 gas with selectivity coefficients of 7.5, 3.67, and 4.69 for acetone, toluene, and ethanol, respectively. The long-term analysis exhibited that the response of this optimum sensor was found to be almost stable. The response of the optimum sensor was decreased by 2.86% after 60 days. The novel findings of this study are highly useful for emerging and future gas sensing devices focused on medical and food industries as well as indoor/outdoor air quality management.

Author contributions

PK contributed to conceptualization, investigation, writing original draft, methodology, software, formal analysis, writing—review and editing; **MG** contributed to formal analysis, writing original draft, software, visualization; **HFH** contributed to supervision, project administration, conceptualization, funding acquisition, writing—review and editing; **VK** contributed to software, visualization; **YKM** contributed to visualization, writing—review and editing. All authors have read and agreed to the published version of the manuscript.

Declaration of competing interest

The authors declare that they have no known competing financial interests.

Data availability statement

All data that support the findings of this study are included within the article (and any supplementary files).

ORCID iDs

Pradeep Kumar https://orcid.org/0000-0001-9635-2489
Monika Gupta https://orcid.org/0000-0003-1502-7401
Huzein Fahmi Hawari https://orcid.org/0000-0001-7152-2277
Yogendra Kumar Mishra https://orcid.org/0000-0002-8786-9379

References

[1] Rodríguez-García S *et al* 2019 Role of the structure of graphene oxide sheets on the CO_2 adsorption properties of nanocomposites based on graphene oxide and polyaniline or Fe_3O_4-nanoparticles *ACS Sustain. Chem. Eng.* **7** 12464–73
[2] Kanaparthi S and Singh S G 2019 Chemiresistive sensor based on zinc oxide nanoflakes for CO_2 detection *ACS Appl. Nano Mater.* **2** 700–6
[3] Ahmad Naseem Z, Manzoor S, Talib M, Islam S S and Mishra P 2020 Self-standing MWCNTs based gas sensor for detection of environmental limit of CO_2 *Mater. Sci. Eng. B Solid-State Mater. Adv. Technol.* **255** 114528
[4] Basyooni M A, Zaki S E, Ertugrul S, Yilmaz M and Eker Y R 2020 Fast response of CO_2 room temperature gas sensor based on mixed-valence phases in molybdenum and tungsten oxide nanostructured thin films *Ceram. Int.* **46** 9839–53
[5] Zaki S E *et al* 2019 Role of oxygen vacancies in vanadium oxide and oxygen functional groups in graphene oxide for room temperature CO_2 gas sensors *Sensors Actuators, A Phys.* **294** 17–24

[6] Khasag N *et al* 2014 Monitoring of exhaled carbon monoxide and carbon dioxide during lung cancer operation *Eur. J. Cardio-thoracic Surg.* **45** 531–6
[7] Varga M, Laposa A, Kulha P, Kroutil J, Husak M and Kromka A 2015 Quartz crystal microbalance gas sensor with nanocrystalline diamond sensitive layer *Phys. Status Solidi Basic Res.* **252** 2591–7
[8] Muckley E S *et al* 2019 Hierarchical TiO_2:Cu_2O nanostructures for gas/vapor sensing and CO_2 sequestration *ACS Appl. Mater. Interf* **11** 48466–75
[9] Alassi A, Benammar M and Brett D 2017 Quartz crystal microbalance electronic interfacing systems: a review *Sensors (Switzerland)* **17** 1–41
[10] Berouaken M *et al* 2018 Quartz crystal microbalance coated with vanadium oxide thin film for CO_2 gas sensor at room temperature *Arab. J. Sci. Eng.* **43** 5957–63
[11] Mardiana L, Wardoyo Masruroh A Y P and Dharmawan H A 2023 A study of an n-TiO_2 coated QCM sensors response and reversibility under CO_2 exposure *Polish J. Environ. Stud.* **32** 1735–42
[12] Malhotra J S, Kubus M, Pedersen K S, Andersen S I and Sundberg J 2023 Room-temperature monitoring of CH_4 and CO_2 using a metal-organic framework-based QCM sensor showing inherent analyte discrimination *ACS Sens.* **8** 3478–86
[13] Kim D Y, Kang H, Choi N J, Park K H and Lee H K 2017 A carbon dioxide gas sensor based on cobalt oxide containing barium carbonate *Sensors Actuators, B Chem.* **248** 987–92
[14] Bhat N *et al* 2023 GO/CuO nanohybrid-based carbon dioxide gas sensors with an arduino detection unit *ACS Omega* **8** 32512–9
[15] Wimmer-Teubenbacher R, Sosada-Ludwikowska F, Zaragoza Travieso B, Defregger S, Tokmak O, Niehaus J S, Deluca M, Köck A *et al* 2018 CuO thin films functionalized with gold nanoparticles for conductometric carbon dioxide gas sensing *Chemosensors* **6** 56
[16] Kayahan E 2018 Porous silicon based CO_2 sensors with high sensitivity *Optik (Stuttg)* **164** 271–6
[17] Gupta M, Hawari H F, Kumar P, Burhanudin Z A and Tansu N 2021 Functionalized reduced graphene oxide thin films for ultrahigh CO_2 gas sensing performance at room temperature *Nanomaterials* **11** 1–18
[18] Young S-J and Lin Z-D 2017 Sensing performance of carbon dioxide gas sensors with carbon nanotubes on plastic substrate *ECS J. Solid State Sci. Technol.* **6** 72–4
[19] Norzam W A S, Hawari H F , Kamarudin K, Juffry Z H M, Hussein N A A, Gupta M and Abdullah A N 2023 Mobile robot gas source localization using SLAM-GDM with a graphene-based gas sensor *Electronics* **12** 171
[20] Gao G *et al* 2016 Heat-initiated chemical functionalization of graphene *Sci. Rep.* **6** 1–8
[21] Wan Q, Guo H and Lin S 2022 Corrugation-induced active sites on pristine graphene for H_2 activation *ACS Catal.* **12** 14601–8
[22] Paul R K, Badhulika S, Saucedo N M and Mulchandani A 2012 Graphene nanomesh as highly sensitive chemiresistor gas sensor *Anal. Chem.* **84** 8171–8
[23] You Y *et al* 2017 On the mechanism of gas adsorption for pristine, defective and functionalized graphene *Phys. Chem. Chem. Phys.* **19** 6051–6
[24] Shaban M, Ali S and Rabia M 2019 Design and application of nanoporous graphene oxide film for CO_2, H_2, and C_2H_2 gases sensing, *J. Mater. Res. Technol.* **8** 4510–20
[25] Kumar R and Kaur A 2020 Chemiresistive gas sensors based on thermally reduced graphene oxide for sensing sulphur dioxide at room temperature *Diam. Relat. Mater.* **109** 108039
[26] Velasco-Soto M A, Pérez-García S A, Alvarez-Quintana J, Cao Y, Nyborg L and Licea-Jiménez L 2015 Selective band gap manipulation of graphene oxide by its reduction with mild reagents *Carbon N. Y.* **93** 967–73
[27] Yang H, Li J S and Zeng X 2018 Correlation between molecular structure and interfacial properties of edge or basal plane modified graphene oxide *ACS Appl. Nano Mater.* **1** 2763–73
[28] Pei S and Cheng H-M 2012 The reduction of graphene oxide *Carbon N. Y.* **50** 3210–28
[29] Musa N, Halim N F A, Ahmad M N, Zakaria Z and Hashim U 2017 Electrical characterization of reduced graphene oxide (rGO) on organic thin film transistor (OTFT) *AIP Conf. Proc.* **1808** 020035–1–020035-7
[30] Chakraborty S, Resmi A N, Devi P R and Jinesh K B 2017 P-channel thin film transistors using reduced graphene oxide *Nanotechnology* **28** 155201
[31] Guo L *et al* 2018 Improved NO_2 gas sensing properties of graphene oxide reduced by two-beam-laser interference *Sci. Rep.* **8** 1–7 [Online]. Available:
[32] Chen C, Chen Y C, Hong Y T, Lee T W and Huang J F 2018 Facile fabrication of ascorbic acid reduced graphene oxide-modified electrodes toward electroanalytical determination of sulfamethoxazole in aqueous environments *Chem. Eng. J.* **352** 188–97 [Online]. Available:
[33] Yuan W *et al* 2013 The edge- and basal-plane-specific electrochemistry of a single-layer graphene sheet *Sci. Rep.* **3** 1–7
[34] Aunkor M T H, Mahbubul I M, Saidur R and Metselaar H S C 2016 The green reduction of graphene oxide *RSC Adv.* **6** 27807–25
[35] Kumuda S, Gandhi U, Mangalanathan U and Rajanna K 2024 Synthesis and characterization of graphene oxide and reduced graphene oxide chemically reduced at different time duration *J. Mater. Sci., Mater. Electron.* **35** 637
[36] Lesiak B *et al* 2021 Chemical and structural properties of reduced graphene oxide—dependence on the reducing agent *J. Mater. Sci.* **56** 3738–54
[37] Minitha C R, Anithaa V S, Subramaniam V and Rajendra Kumar R T 2018 Impact of oxygen functional groups on reduced graphene oxide-based sensors for ammonia and toluene detection at room temperature *ACS Omega* **3** 4105–12
[38] Bhattacharya G, Sas S, Wadhwa S, Mathur A, McLaughlin J and Roy S S 2017 Aloe vera assisted facile green synthesis of reduced graphene oxide for electrochemical and dye removal applications *RSC Adv.* **7** 26680–8
[39] Gupta M, Athirah N and Hawari H F 2020 Graphene derivative coated QCM-based gas sensor for volatile organic compound (VOC) detection at room temperature *Indones. J. Electr. Eng. Comput. Sci.* **18** 1279–86
[40] Kumar P, Kang C H, Burhanudin Z A, Saheed M S M, Irshad M I and Mohamed N M 2016 Graphene-based hybrid thin films as transparent conductive electrode for optoelectronic devices *IEEE Int. Conf. on Semiconductor Electronics, Proc., ICSE* vol. 2016-Sept 216–9
[41] Bo Z *et al* 2014 Green preparation of reduced graphene oxide for sensing and energy storage applications *Sci. Rep.* **4** 1–8
[42] Kumar P, Lin K, Seng W, Shuaib M and Saheed M 2019 Hybrid film of single-layer graphene and carbon nanotube as transparent conductive electrode for organic light emitting diode *Synth. Met.* **257** 116186
[43] Bhaumik A *et al* 2017 Reduced graphene oxide thin films with very large charge carrier mobility using pulsed laser deposition *J. Mater. Sci. Eng.* **06** 1000364
[44] Kumar P *et al* 2022 Surface-treatment process related sheet resistance variations in graphene-based thin-film electrodes *Surfaces and Interfaces* **32** 102161

[45] Ferrari A C *et al* 2015 Science and technology roadmap for graphene, related two-dimensional crystals, and hybrid systems *Nanoscale* **7** 4598–810
[46] Ferrari A C and Basko D M 2013 Supplly Raman spectroscopy as a versatile tool for studying the properties of graphene *Nat. Nanotechnol.* **8** 235–46
[47] Li J, Zhao H, Wang Y and Zhou Y 2024 Approaches for selectivity improvement of conductometric gas sensors: an overview *Sensors and Diagnostics* **3** 336–53
[48] Triyana K *et al* 2019 A highly sensitive safrole sensor based on polyvinyl acetate (PVAc) nanofiber-coated QCM *Sci. Rep.* **9** 1–12
[49] Kim J H *et al* 2019 Enhancement of H2S sensing performance of p-CuO nanofibers by loading p-reduced graphene oxide nanosheets *Sensors Actuators, B Chem.* **281** 453–61
[50] Kumar P, Hawari H F, Gupta M, Xian W and Leong R 2024 Comparative investigation of surface-electrical properties of functionalized graphene and MXene thin films for CO_2 gas sensing *J. Mater. Sci.* **59** 22132–48